Accepted Manuscript

FPZ evolution of mixed mode fracture in concrete: Experimental and numerical

Wei Dong, Zhimin Wu, Xiangming Zhou, Liheng Dong, Gediminas Kastiukas

Please cite this article as: Wei Dong, Zhimin Wu, Xiangming Zhou, Liheng Dong, Gediminas Kastiukas , FPZ evolution of mixed mode fracture in concrete: Experimental and numerical. The address for the corresponding author was captured as affiliation for all authors. Please check if appropriate. Efa(2016), doi: 10.1016/j.engfailanal.2017.01.017

FPZ Evolution of Mixed Mode Fracture in Concrete: Experimental and Numerical

Wei Dong[1], Zhimin Wu[2,*], Xiangming Zhou[3], Liheng Dong[4], Gediminas Kastiukas[5]

[1]Associate Professor, State Key Laboratory of Coastal and Offshore Engineering, Dalian University of Technology & Ocean Engineering Joint Research Center of DUT-UWA, Dalian 116024, P. R. China. E-mail: dongwei@dlut.edu.cn

[2]Professor, State Key Laboratory of Coastal and Offshore Engineering, Dalian University of Technology, Dalian 116024, P. R. China.

 (*Corresponding author): E-mail: wuzhimin@dlut.edu.cn

[3]Reader in Civil Engineering Design, Department of Mechanical, Aerospace and Civil Engineering, Brunel University London, Uxbridge, UB8 3PH, UK & Haitian Visiting Professor, State Key Laboratory of Coastal and Offshore Engineering, Dalian University of Technology, Dalian 116024, P. R. China. E-mail: xiangming.zhou@brunel.ac.uk

[4]Postgratuate student, State Key Laboratory of Coastal and Offshore Engineering, Dalian University of Technology, Dalian 116024, P. R. China. E-mail: lhdong@163.com

[5]PhD student, Department of Mechanical, Aerospace and Civil Engineering, Brunel University London, Uxbridge, UB8 3PH, UK. Email: Gediminas.Kastiukas@brunel.ac.uk

ABSTRACT

Digital image correlation (DIC) technique is applied to study the evolution of fracture process zone (FPZ) of mixed mode fracture in concrete. By testing a series of beams of various sizes under four-point shearing, the opening and sliding displacements on the crack surfaces are derived using the DIC technique. Meanwhile, a numerical method is employed to simulate

the fracture process by introducing a crack propagation criterion. The opening and sliding displacements on the crack surfaces obtained from numerical analysis exhibit a reasonable agreement with the experimental results, which verifies the DIC technique presented in the study. By combining experimental observations with numerical simulations, the evolution of the FPZ during the whole crack propagation process of mix mode fracture is investigated and elaborated in depth. The results indicate that the ratio of crack opening to sliding displacement remains approximately constant as crack propagates before reaching a peak load. Meanwhile, the FPZ evolution during the complete fracture process is influenced by the specimen ligament length and the ratio of mode I to II stress intensity factor component. With the decrease of ligament length and the ratio of mode I to II stress intensity factor component, the full FPZ length decreases. However, when the ligament length is less than 63 mm or ratio of mode I to II stress intensity factor component is less than 0.11, the FPZ cannot fully develop, but keeps increasing as crack propagates.

Keywords: concrete, mixed mode fracture, fracture process zone, digital image correlation, numerical simulation

Introduction

Macro-crack propagation in cementitious materials, such as concrete, is caused by the initiation, micro-crack coalescence, and development of the fracture process zone (FPZ), which usually exists ahead of the crack tip. The existence of the FPZ reflects the strain localization and nonlinear properties of quasi-brittle materials like concrete, which is essentially different from the scenario for brittle materials. As a consequence, some

fundamental fracture properties of concrete, including fracture energy and critical fracture toughness, are affected by the evolution of the FPZ. Particularly, the applicability of linear fracture mechanics in structure analysis is determined by the FPZ length and structural size. Therefore, the study of FPZ properties in concrete has attracted great attention from science and engineering communities.

So far, most experimental and theoretical studies concerning the FPZ evolution of concrete have focused on mode I fracture. Wu et al. [1] conducted an experimental study on the FPZ development in beams of various sizes under three-point bending (TPB) and concluded that the FPZ length increases at the early stage of crack propagation while decreases after the FPZ fully develops. Dong et al. [2] developed a numerical method to study the FPZ properties by introducing the initial fracture toughness and pointed out that there are three cases for the variation of FPZ length depending on the initial crack ratios (a_0/H, where a_0 is the initial crack length and H is the specimen height). Skarżyński et al. [3] observed the shape and width of FPZ using a digital image correlation (DIC) technique and developed a numerical method [4] to explore the effects of characteristic length and aggregates size on the width and shape of the FPZ. The studies mentioned above provided quantitative information for deeper understanding of the non-linear behavior and explored the failure mechanism of concrete structures.

However, in many engineering structures in the field, e.g. gravity dams, the crack tip is usually under the mixed mode I-II stress condition rather than under a pure mode I stress condition [5]. In the case of mixed mode I-II fracture, the tensile and shearing combination stress field at the crack tip results in the cracking opening and sliding displacements during

fracture process. Therefore, the FPZ evolution under mixed mode I-II fracture also affects the crack propagation trajectory and failure mode of concrete structures. To better understand the crack propagation of mixed mode I-II fracture in concrete, experimental and numerical studies have been conducted in previous decades. The single [6-8] and double notched four-point shearing (FPS) tests [9] were carried out to investigate structural responses, including cracking mouth opening and sliding displacements (CMOD and CMSD), loading point displacement and cracking trajectory. Later, the FPS beams with one/double notches became the benchmark for verifying the numerical method for the crack propagation analysis of mixed-mode fracture in concrete [10-14]. Meanwhile, to reflect the actual stress condition for concrete dams in service, model dam tests were carried out by other researchers [10, 15]. Similar to the FPS tests, the macro-responses of the dams were targeted so that the load (P) vs CMOD/CMSD curves could be derived in the model experiments. Correspondingly, the experimental results were also employed for the purpose of mixed-mode crack propagation analysis using numerical methods [10, 16, 17]. However, it should be noted that the objectives of these experimental studies were to obtain the nonlinear behaviors of the structures at a macro-level, rather than to observe the micro-crack initiation and the FPZ evolution. In fact, from an in-depth insight into mixed-mode fracture mechanisms in concrete, the development of the FPZ reflects the cohesive characteristics and strain localization under complex stress conditions. Therefore, the research on FPZ properties provides scientific evidences for developing theoretical and numerical methods to study the fracture failure of concrete structures under complex stress field. The experimental results can also provide a promising way for verifying an analytical or

numerical model.

With the development of more innovative optical measurement methods, DIC technique has been implemented to characterize the fracture process by providing a high-resolution measurement of the full-field displacements of cracking surface. It has previously been employed to study the crack propagation of mode I fracture [1, 18, 19], concrete-concrete interfacial fracture [20] and carbon fiber reinforced polymers (CFRP)-concrete interfacial fracture [21]. Regarding the mixed mode fracture in a single component, Lin et al. [22] studied the fracture process in quasi-brittle materials by taking sandstone as an example. For the case of concrete under mixed-mode fracture, to the best knowledge of the authors, no reported experimental study exists on FPZ evolution during the fracture process. Meanwhile, it should be noted that compared to mode I fracture, concrete under mixed-mode fracture exhibits higher brittleness, making it difficult to obtain a structure's responses at post-peak loading stage. Therefore, in this study, a combined experimental and numerical method is adopted to analyze the FPZ evolution of mixed mode I-II fracture in concrete. Firstly, the DIC technique is used to derive the evolution of FPZ until reaching the peak load. The crack propagation trajectory and opening/sliding displacements on the crack surfaces are recorded on FPS specimens with the same initial mixty ratio K_I/K_{II}. Here, K_I and K_{II} are the stress intensity factors (SIFs) for modes I and II, respectively. A numerical method is introduced to analyze the whole fracture process, which is verified by the results from DIC experiment. Finally, the FPZ evolution of mixed mode I-II fracture during a complete crack propagation process is discussed in depth based on the numerical results.

Experimental Program

Specimen Preparation and Experimental Setup

Four groups of beams with depths of 60, 90, 120 and 150 mm, respectively, were tested under FPS. The specimens with the asterisk in Table 1 were tested in combination with measurement by using the DIC technique. The geometry and loading arrangement of the beams are illustrated in Fig. 1. Here, *H, B and L* are the height, width and length of the beams, respectively; *C, L_1* and *C_1* are the distances from the two loading points and pre-notch, respectively, to the geometric center of the specimens. It should be noted that the initial mixty ratio K_I^{ini}/K_{II}^{ini} is set as 1.6 for all the beams from all four size groups by adjusting the pre-notch and loading positions (See Table 1). K_I^{ini} and K_{II}^{ini} are the SIFs of modes I and II, respectively, corresponding to the crack initiation.

The concrete mix proportions for this study were 1: 2.77: 4.16: 0.72 (cement: sand: aggregate: water) by weight and the maximum aggregate size was 10 mm. The measured material properties of concrete are as following: cubic compressive strength f_{cu} = 29.3 MPa, splitting tensile strength f_t = 2.54 MPa, Young's modulus E_c = 28.0 GPa, Poisson's ratio v = 0.18, fracture energy G_f = 138.6 N/m, and initial mode I fracture toughness of K_{IC}^{ini} = 0.56 MPa·m$^{1/2}$.

A closed loop servo-controlled testing machine with a compression loading capacity of 250 kN was used for loading the beam specimens. For each specimen, a clip gauge was mounted on the bottom of the beam to measure the crack mouth displacements (CMD). The tests were performed under displacement control mode with a displacement rate of 0.005 mm/s.

Digital Image Correlation Technique

DIC is a powerful optical and non-contact measuring technique, which is usually employed to analyze two-dimensional deformations on a specimen surface. By comparing the deformed images with the reference image before deformation, the deformation of a specimen caused by the applied load can be derived using the DIC technique. Compared with traditional measurement techniques, it shows advantages on visualizing surface deformation of concrete specimen. Firstly, DIC technique is a non-contact test method, which ensures that the crack surface displacement is not interfered by experiment devices [1, 23]. Moreover, the DIC images corresponding to various loading stages can be recorded and processed conveniently, so that it is possible to be used on the measurements for a large number of specimens. Finally, according to the different experimental objectives, the DIC technique can be used for the displacement measurement in the surfaces of various objects [21, 24]. However, it should be noted that DIC technique can only capture the two-dimensional plane deformation so that it is not convenient for the analysis of three-dimensional problems.

In this study, the specimen surface was polished before testing, and a speckle pattern (serving as a tracer in DIC) was made on the specimen surface using standard black spray paint. Figs. 2(a), (b) and (c) showed the speckle pattern on specimen surface, DIC set-up and measurement devices under FPS in the experiment, respectively. Digital images were obtained at a rate of one set per second using a digital camera with a resolution of 1024×768 pixels during loading. Considering that the crack trajectory is not perpendicular to horizontally neutral axis of a beam section, the computational domain moves to the potential

crack propagation direction. Taking Specimen L150-1 as an example, the tip of the pre-crack is located at the origin of the coordinate plane, i.e. Point O. By picking up one out of each five pixels (1 pixel = 0.112 mm for Specimen L150, which the precision is 0.001 mm), a computational grid with 27313 (143×191) points was selected to conduct the deformation analysis in the u (perpendicular to the pre-crack surface) and v (parallel to the pre-crack surface) directions (See Fig. 3). In Fig. 3, Line MN is just above the tip of a pre-crack, and Lines M_1N_1, M_2N_2……, M_nN_n (n = 191) are parallel to Line MN with an interval of 5 pixels. By capturing the jump of the grid points along a particular loading moment, the opening displacement along the u direction, denoted as w_1, and the sliding displacement along the v direction, denoted as w_2, can be obtained. Taking Specimen L120-1 as an example, Fig. 4(a) and (b) illustrate the opening and sliding displacements along Line MN when $P = 96.7\%P_{max}$. The displacement jump points are denoted as Points Q and R, which represent the deformation edges. So they can be used to define the crack profile on line MN corresponding to the loading Point $P = 96.7\%P_{max}$. At that moment, the difference of w_1-values at Points Q and R in Fig. 4(a) corresponds to the opening displacement on Line MN. Accordingly, the difference of w_2-values at Points Q and R in Fig. 4(b) corresponds to the sliding displacement on Line MN. Then, since the opening/sliding displacements on line MN are obtained at the loading Point $P = 96.7\%P_{max}$, the crack profile on line MN at that moment can be derived. Accordingly, the profile along the whole crack can be obtained using the above-mentioned process by deriving the opening/sliding displacements on lines M_1N_1, M_2N_2……M_nN_n. In a similar manner, opening/sliding displacements and the crack profile are obtained for every point on the *P-CMOD* curve. As a result, the opening/sliding

displacements and the relative FPZ length during the fracture process of concrete can be obtained.

Numerical Program

Compared with mode I fracture, the component of mode II exists in the mixed mode I-II fracture, resulting in increased brittleness in concrete specimens under FPS. In this study, the load vs displacement curves at post-peak loading stage are not collected due to sudden fracture occurrence. Therefore, the FPZ evolution after peak load is studied using a numerical method, for which a crack propagation criterion is introduced to determine the crack propagation. This criterion can be described as following: crack propagation is initiated when the difference, between the SIFs caused by the applied load and by the cohesive stress, satisfies the crack initiation criterion. The crack propagation criterion has been established and validated by Wu et al. [10], and has been found to be able to predict the whole fracture process of concrete with respect to mode I fracture [2, 25-27] and mixed mode I-II fracture [10] as well as the fracture process of rock-concrete interface [28]. By combining with the maximum circumferential stress criterion [29], the crack propagation criterion used in this study can be expressed by Eq. (1) as follows:

$$K_{I,II}(P,\sigma) = \cos\frac{\theta}{2}\left[(K_I^P - K_I^\sigma)\cos^2\frac{\theta}{2} - \frac{3}{2}(K_{II}^P - K_{II}^\sigma)\sin\theta\right] = K_{IC}^{ini} \tag{1}$$

with $\quad \theta = 2\arctan\frac{1}{4}\left[(K_I^P - K_I^\sigma)/(K_{II}^P - K_{II}^\sigma) \pm \sqrt{(K_I^P - K_I^\sigma)^2/(K_{II}^P - K_{II}^\sigma)^2 + 8}\right]$ $\tag{2}$

where K_I^P and K_{II}^P are the SIFs of modes I and II respectively caused by an applied load while K_I^σ and K_{II}^σ are the SIFs of modes I and II respectively caused by the cohesive stress. K_{IC}^{ini} is the initial fracture toughness of mode I in concrete, which can be determined by

giving the initial cracking load P_{ini} and a_0 [30, 31].

The crack propagation angle α is determined using Eq.(3) as

$$\alpha = \frac{1}{2}\arctan\frac{\gamma_{xy}}{\varepsilon_x - \varepsilon_y} \tag{3}$$

where ε_x and ε_y are normal strains at the crack tip along the x and y directions, respectively. γ_{xy} is the shear strain at the tip of the crack.

A bilinear relationship between cohesive stress (σ) with the crack opening displacement (w) is adopted in the numerical analysis which is formulated as follows:

$$\sigma = f_t - (f_t - \sigma_s)\frac{w}{w_s} \qquad \text{for } 0 \leq w \leq w_s \tag{4}$$

$$\sigma = \sigma_s\frac{w_0 - w}{w_0 - w_s} \qquad \text{for } w_s < w \leq w_0 \tag{5}$$

$$\sigma = 0 \qquad \text{for } w > w_0 \tag{6}$$

According to Petersson [32], σ_s, w_s and w_0 can be determined as follows:

$$\sigma_s = f_t/3 \tag{7}$$

$$w_s = 0.8G_f/f_t \tag{8}$$

$$w_0 = 3.6G_f/f_t \tag{9}$$

where w_s and σ_s are the crack opening displacement and the corresponding cohesive stress respectively at the break-point of the bilinear σ-w relationship and w_0 is the stress-free crack opening displacement (See Fig. 5). It should be noted that, in the case of mixed-mode fracture, the crack opening displacement w consists of a normal component, w_1, and a tangential component, w_2. In this study, it is assumed that w affects the energy dissipation and is associated with the cohesive stress. As a consequence, the end of the FPZ is determined by a comparison of w with w_0. According to the experimental results

aforementioned, G_f and f_t of the concrete are 138.6 N/m and 2.54 MPa, respectively. Thus, w_0 is 0.196 mm from Eq. (9).

The crack propagation criterion above mentioned is employed to analyze the complete fracture process through using an iterative process, which is illustrated by the program flow diagram shown in Fig. 6. The numerical procedure is shown in the following steps.

1. Input data, $P(1) = P_{ini}$, $a(1) = a_0$. Calculate $\alpha(1)$ based on P_{ini} from the experiment.

2. Establish FEM model for FPS beam with crack length $a_{i,j} = a(j-1) + \Delta a$ ($i = 1,2…$, $j = 2,3…$) and crack propagation angle $\alpha(j-1)$. Here Δa is a specified increment of crack length. i represents the load increment during the iteration process with a same crack length. j represents the crack length increment during the iteration analyses.

3. Apply load $P_{i,j}$ to the FPS beam and calculate cohesive stress $\sigma_{i,j}$ using Eqs. (4)-(6). Calculate K_I^P, K_I^σ, K_{II}^P and K_{II}^σ by adjusting load $P_{i,j}$ until Eq. (1) is satisfied. Calculate $\alpha(j)$ using Eq. (3).

4. Repeat steps 2-3 for the next crack propagation. The iterative process terminates when the crack tip is closed to the boundary of the beam or the value of the corresponding applied load becomes negative.

Therefore by repeating this exercise, the whole fracture process can be obtained numerically. Details of the iterative numerical process for predicting crack propagation based on the crack propagation criterion can be referred to Reference[10].

Figs. 7 and 8 illustrate the comparisons of *P-CMD* curves and crack trajectories between the experimental and numerical results, in which the shaded areas consist of envelope curves from the experimental results. It can be seen that the numerical results show

reasonable agreements with the experimental data. It verifies that the employed numerical method, adopted in this paper, can effectively simulate the crack propagation process and reflect the fracture characteristics of concrete under FPS. Therefore, to fill the gap that fails to achieve the complete fracture process during experiment, the FPZ evolution at post-peak load stage is studied using the verified numerical method.

Results and Discussions

Evolution of the FPZ Based on Experimental Results

Based on the experimental results of DIC, Figs. 9 to 12 illustrate the FPZ evolution of Specimens L60-1, L90-1, L120-1 and L150-1, respectively, during the whole loading process. Since the crack trajectory under FPS is curvilinear, the Y-coordinate demonstrates the crack trajectory length in these figures. It can be seen that the distribution of w_1 (i.e. the opening displacement) along the crack surface is approximately linear. However, the scenario is different in the case of w_2 (i.e. sliding displacement), which exhibits an approximately bilinear distribution. The breakpoint position is at around 1/3-1/2 of the length of the FPZ.

Fig. 13 illustrates the variation of initial crack tip opening and sliding displacements (*CTOD* and *CTSD*) at various loading stages. The results show that the ratios of *CTSD* to *CTOD* are kept approximately constant for the different size specimens with respect to various loading stages. According to the reports in literature [8, 10, 22], the fracture mode will be increasingly mode I dominated as crack propagates. However, it seems that the ratios of *CTSD* to *CTOD* are not significantly influenced by the variation of fracture mode before the post-peak loading stage. The sliding displacement increases at the same rate as the

opening displacement.

Meanwhile, Fig. 14 shows the ratios of $L_{FPZ}/(H\text{-}a_0)$ at peak load for various specimen sizes. Here, L_{FPZ} denotes the length of FPZ, which is equal to the crack propagation length from the fictitious crack tip to the starting point of free-stress crack. By means of DIC, the fictitious crack tip and the starting point of free-stress crack can be captured through calculating the displacement field along the crack propagation trajectory. As a result, L_{FPZ} can be determined before post-peak loading stage in experiment. It can be seen that the ratios are all in similar values, ranging between 0.34 to 0.38, for the FPS beams with heights of 60, 90, 120 and 150 mm. As a consequence, it can be concluded that the specimen size under FPS has an obvious effect on the critical L_{FPZ} (See Figs. 9 to 12), but less on the relative critical FPZ length, i.e. $L_{FPZ}/(H\text{-}a_0)$.

FPZ Properties during the Complete Fracture Process Based on the Numerical Results

According to the fictitious crack model [33], the FPZ will fully develop when the initial crack tip displacement exceeds w_0. In the case of concrete mode I fracture, this has already been reported in experimental [1] and numerical [2] studies. In this section, the FPZ properties during the complete fracture process will be discussed based on the numerical results.

First, the L-Series specimens were taken as an example to analyze the effect of specimen height on FPZ properties. The sizes and loading conditions of L-Series specimens are listed in Table 1, in which the heights vary from 60 to 150 mm, and a_0/H and K_I^{ini}/K_{II}^{ini} are kept as 0.3 and 1.6, respectively. Table 2 lists the numerical results of L_{FPZ} and initial crack tip displacement (*CTD*, which is equal to $\sqrt{CTOD^2 + CTSD^2}$) at the final crack propagation step

for L-Series specimens. It should be noted that the load will decrease to zero after this step. For the Specimens L60 and L90, the FPZs do not fully develop ($CTD < w_0$) even the specimens reach ultimate failure, i.e. the applied loads decrease to zero. Therefore, the FPZ length increases uniformly as the crack propagates (See Fig. 15), rather than decreasing after reaching a peak as the scenario under three-point bending (i.e. TPB) [1]. However, the scenario is different in the case of the Specimens L120 and L150. The FPZs fully develop ($CTD > w_0$) as the crack propagates. As a consequence, the FPZ length increases to the peak, i.e. the full FPZ length, and starts decreasing after that. Meanwhile, with the increase in specimen height, the full FPZ length, L_{FPZ}^{F}, increases, while the corresponding $L_{FPZ}^{F}/(H\text{-}a_0)$ decreases.

The S-Series specimens were used as an example to analyze the effect of a_0/H on FPZ properties. The sizes and loading conditions of S-Series specimens are listed in Table 3, for which a_0/H varies from 0.2 to 0.6 while the heights and K_I^{ini}/K_{II}^{ini} are kept constant at 150 mm and 1.6, respectively. The numerical results of L_{FPZ} and CTD listed in Table 3 correspond to the final crack propagation step in S-Series specimens. Meanwhile, the FPZ evolution in S-Series specimens is illustrated in Fig. 16. It can be seen from this figure that the FPZ does not fully develop for the specimen S150-5 with a_0/H of 0.6, i.e. the FPZ length keeps increasing linearly as the crack propagates. With the decrease of a_0/H from 0.5 to 0.2, the FPZ can fully develop and begins to decrease thereafter. Moreover, with the decline of a_0/H, the full FPZ length, L_{FPZ}^{F}, increases, while the corresponding $L_{FPZ}^{F}/(H\text{-}a_0)$ decreases.

It is worthy to point out that both varying the specimen height by fixing a_0/H and varying a_0/H by fixing the specimen height can directly change the ligament length of specimens. For the

specimens without the development of the full FPZ, i.e., Specimens L60, L90 and S150-5, the ligament lengths are 42, 63 and 60 mm, respectively. For the other specimens in the L and S Series with the minimum ligament length of 75 mm, the FPZ can fully develop. By arranging the FPZ evolution curves according to the variation of ligament lengths as presented in Fig. 17, it can be concluded that it is the ligament length that affects the FPZ evolution under FPS with the same $K_{\mathrm{I}}^{\mathrm{ini}}/K_{\mathrm{II}}^{\mathrm{ini}}$. With the decrease of ligament length, the full FPZ length, L_{FPZ}^{F}, decreases, while the corresponding $L_{FPZ}^{F}/(H_0\text{-}D)$ increases. When the ligament length decreases to a certain value, which is 63 mm in this study, FPZ cannot fully develop.

The T-Series specimens were used as an example to analyze the effect of modes I and II stress intensity factor components on FPZ properties. The sizes and loading conditions of T-Series specimens are listed in Table 4, in which $K_{\mathrm{I}}^{\mathrm{ini}}/K_{\mathrm{II}}^{\mathrm{ini}}$ varies from 0.11 to infinity, i.e. pure mode I fracture while the heights and a_0/H are kept constant at 150 mm and 0.3, respectively. The numerical results of L_{FPZ} and CTD listed in Table 4 correspond to the final crack propagation step in T-Series specimens. Meanwhile, the FPZ evolution for T-Series specimens is illustrated in Fig. 18. For the specimen T150-1 with $K_{\mathrm{I}}^{\mathrm{ini}}/K_{\mathrm{II}}^{\mathrm{ini}}$ of 0.11, which can be regarded as being approximately mode II fracture dominated, the FPZ is not fully developed. Therefore, it can be concluded that together with the specimen ligament length, the proportion of initial stress intensity factor components of modes I and II affects the FPZ characteristics, including the evolution process and length, as the crack propagates.

Conclusions

The concrete crack propagation process of mixed mode fracture and its corresponding

variations of crack surface displacements before the peak load stage were experimentally studied using DIC technique. To analyze the FPZ evolution during the complete fracture process, a numerical method was employed to simulate the evolution of FPZ under FPS. By comparing with the experimental results, the numerical method was validated. Furthermore, the effects of specimen size, a_0/H and $K_{\mathrm{I}}^{\mathrm{ini}}/K_{\mathrm{II}}^{\mathrm{ini}}$ on the variations of FPZ with respect to crack propagation were discussed based on the numerical results. According to the experimental and numerical studies, the following conclusions can be drawn:

1. The experimental results showed that, before the peak load, the ratios of *CTSD* to *CTOD* remain approximately constant for the specimens with different sizes but the same $K_{\mathrm{I}}^{\mathrm{ini}}/K_{\mathrm{II}}^{\mathrm{ini}}$. They do not change with variations in fracture mode as crack propagates. Meanwhile, the distribution of the opening displacement along the crack surface is approximately linear, and that of sliding displacement is approximately bilinear, with the breakpoint position at approximate 1/2-1/3 length of the FPZ.

2. Based on the numerical results, the FPZ length either starts to decrease after reaching a peak, i.e. after the FPZ fully develops, or increases monotonously until final failure of a specimen. Different processes of the FPZ evolution are determined by the ligament length and $K_{\mathrm{I}}^{\mathrm{ini}}/K_{\mathrm{II}}^{\mathrm{ini}}$ for mixed mode fracture in concrete.

3. Although both a_0/H and specimen size affect the FPZ length, it is the ligament length that affects the FPZ evolution for the specimens with the same $K_{\mathrm{I}}^{\mathrm{ini}}/K_{\mathrm{II}}^{\mathrm{ini}}$. In this study, with a decrease of the ligament length from 120 to 75 mm, the full FPZ length decreases, while the ratio of $L_{FPZ}^{F}/(H_0\text{-}D)$ increases. When the ligament is less than 63 mm, the FPZ cannot fully develop, and keeps increasing as the crack propagates.

4. For the specimens with a height of 150 mm and a_0/H of 0.3, the ratios of K_I^{ini}/K_{II}^{ini} determine the FPZ evolution. In the case of K_I^{ini}/K_{II}^{ini} = 0.11, which is approximately mode II dominated fracture, the FPZ cannot fully develop. With the increase of K_I^{ini}/K_{II}^{ini} from 0.66 to infinity, i.e. corresponding to mode I fracture, the full FPZ lengths decrease. It demonstrates that the crack propagation resistance will increase with the increase in the mode II component in mixed mode I-II fracture.

Acknowledgement

References

[1] Wu Z, Rong H, Zheng J, Xu F, Dong W. An experimental investigation on the FPZ properties in concrete using digital image correlation technique. Eng Fract Mech. 2011;78:2978-90.

[2] Dong W, Zhou X, Wu Z. On fracture process zone and crack extension resistance of concrete based on initial fracture toughness. Constr Build Mater. 2013;49:352-63.

[3] Skarżyński Ł, Syroka E, Tejchman J. Measurements and calculations of the width of the fracture process zones on the surface of notched concrete beams. Strain. 2011;47:319-32.

[4] Skarżyński Ł, Tejchman J. Calculations of fracture process zones on meso-scale in notched concrete beams subjected to three-point bending. Eur J Mech A-solid. 2010;29:746-60.

[5] Bocca P, Carpinteri A, Valente S. Mixed-mode fracture of concrete. Int J Solids Struct. 1991;27:1139-53.

[6] Arrea M, Ingraffea AR. Mixed-mode crack propagation in mortar and concrete. Rep. No. 81-13, Dept. of Structural Engineering, Cornell Univ. Ithaca, NY; 1982.

[7] Barpi F, Valente S. Size-effects induced bifurcation phenomena during multiple cohesive crack propagation. Int J Solids Struct. 1998;35:1851-61.

[8] Carpinteri A, Valente S, Ferrara G, Melchiorri G. Is mode-II fracture energy a real material property? Comput Struct. 1993;48:397-413.

[9] Bocca P, Carpinteri A, Valente S. Size effect in the mixed-mode crack propagation-softening and snap back analysis. Eng Fract Mech. 1990;35:159-70.

[10] Wu Z, Rong H, Zheng J, Dong W. Numerical method for mixed mode I–II crack propagation in concrete. J Eng Mech, ASCE. 2013;139:1530-8.

[11] Ooi ET, Yang ZJ. A hybrid finite element-scaled boundary finite element method for crack propagation modelling. Comput Method Appl M. 2010;199:1178-92.

[12] Yang ZJ, Xu XF. A heterogeneous cohesive model for quasi-brittle materials considering spatially varying random fracture properties. Comput Method Appl M. 2008;197:4027-39.

[13] Cendón DA, Gálvez JC, Elices M, Planas J. Modelling the fracture of concrete under mixed loading. Int J Fracture. 2000;103:293-310.

[14] Saleh AL, Aliabadi MH. Crack growth analysis in concrete using boundary element mthod. Eng Fract Mech. 1995;51:533-45.

[15] Barpi F, Valente S. Numerical simulation of prenotched gravity dam models. J Eng Mech. 2000;126:611-9.

[16] Dias-da-Costa D, Alfaiate J, Sluys LJ, Julio E. A comparative study on the modelling of discontinuous fracture by means of enriched nodal and element techniques and interface elements. Int J Fracture. 2010;161:97-119.

[17] Barpi F, Valente S. The cohesive frictional crack model applied to the analysis of the dam-foundation joint. Eng Fract Mech. 2010;77:2182-91.

[18] Alam SY, Saliba J, Loukili A. Fracture examination in concrete through combined digital image correlation and acoustic emission techniques. Constr Build Mater. 2014;69:232-42.

[19] Trivedi N, Singh RK, Chattopadhyay J. Investigation on fracture parameters of concrete through optical crack profile and size effect studies. Eng Fract Mech. 2015;147:119-39.

[20] Shah SG, Kishen JMC. Fracture properties of concrete-concrete interfaces using digital image correlation. Exp Mech. 2011;51:303-13.

[21] Corr D, Accardi M, Graham-Brady L, Shah S. Digital image correlation analysis of interfacial debonding properties and fracture behavior in concrete. Eng Fract Mech. 2007;74:109-21.

[22] Lin Q, Yuan H, Biolzi L, Labuz JF. Opening and mixed mode fracture processes in a quasi-brittle material via digital imaging. Eng Fract Mech. 2014;131:176-93.

[23] Helm JD. Digital image correlation for specimens with multiple growing cracks. Exp Mech. 2008;48:753-62.

[24] Huon V, Cousin B, Wattrisse B, Maisonneuve O. Investigating the thermo-mechanical behaviour of cementitious materials using image processing techniques. Cem Concr Res. 2009;39:529-36.

[25] Dong W, Wu Z, Zhou X. Calculating crack extension resistance of concrete based on a

new crack propagation criterion. Constr Build Mater. 2013;38:879-89.

[26] Wu Z, Wu X, Dong W, Zheng J, Wu Y. An analytical method for determining the crack extension resistance curve of concrete. Mag Concr Res. 2014;66:719-28.

[27] Dong W, Wu Z, Zhou X, Wang C. A comparative study on two stress intensity factor-based criteria for prediction of mode-I crack propagation in concrete. Eng Fract Mech. 2016;158:39-58.

[28] Dong W, Wu Z, Zhou X. Fracture mechanisms of rock-concrete interface: experimental and numerical. J Eng Mech, ASCE. 2016;142:04016040.

[29] Erdogan F, Sih GC. On the crack extension in plates under plane loading and transverse shear. Journal of Basic Eng ASME. 1963;85:519-25.

[30] Xu S, Reinhardt H. Determination of double-Determination of double-K criterion for crack propagation in quasi-brittle fracture Part I: Experimental investigation of crack propagation. Int J Fracture. 1999;98:111-49.

[31] Xu S, Reinhardt HW. Determination of double-K criterion for crack propagation in quasi-brittle fracture, Part II: Analytical evaluating and practical measuring methods for three-point bending notched beams. Int J Fracture. 1999;98:151-77.

[32] Petersson PE. Crack growth and development of fracture zones in plain concrete and similar materials. Division of Building Materials, Lund Institute of Technology, Report TVBM-1006, Sweden, 1981. 1981.

[33] Hillerborg A, Modéer M, Petersson PE. Analysis of crack formation and crack growth in concrete by means of fracture mechanics and finite elements. Cem Concr Res. 1976;6:773-81.

Appendix I Tables

Table 1. Specimen geometries and experimental results

Specimen	$L \times H \times B$ (mm^3)	a_0 (mm)	C (mm)	C_1 (mm)	P_{max} (kN)	K_I^{ini} / K_{II}^{ini}
*L60-1					5.41	
L60-2	340×60×40	18	20	25	4.96	
L60-3					5.68	
L60-4					5.31	
*L90-1					9.05	
L90-2	460×90×40	27	30	20	8.92	
L90-3					7.85	
L90-4					7.88	
*L120-1					9.95	1.6
L120-2	580×120×40	36	40	15	10.15	
L120-3					9.02	
L120-4					9.61	
*L150-1					12.93	
L150-2	700×150×40	45	50	10	13.56	
L150-3					11.86	
L150-4					11.69	

Table 2. Numerical results of L-Series specimens

Specimen	L_{FPZ} (mm)	CTD (mm)	w_0 (mm)
L60	42	0.135	
L90	64	0.181	0.196
L120	74	0.213	
L150	86	0.241	

Table 3. Geometries of S-Series specimens and numerical results

Specimen	$L \times H \times B$ (mm×mm×mm)	C (mm)	C_1 (mm)	a_0 (mm)	L_{FPZ} (mm)	CTD (mm)	P_{max} (kN)	K_I^{ini} / K_{II}^{ini}
S150-1			17	30	92	0.185	17.48	
S150-2			25	45	86	0.221	12.28	
S150-3	700×150×40	50	27	60	76	0.228	8.98	1.60
S150-4			28.5	75	66	0.241	6.48	
S150-5			29	90	58	0.278	4.56	

Table 4. Numerical results of T-Series specimens at the final crack propagation step

Specimen	$L \times H \times B$ (mm$\times$mm$\times$mm)	C (mm)	C_1 (mm)	a_0 (mm)	L_{FPZ} (mm)	CTD (mm)	P_{max} (kN)	K_I^{ini} / K_{II}^{ini}
T150-1		50	0		98	0.136	13.66	0.11
T150-2		50	10		86	0.203	12.88	0.66
T150-3	$700 \times 150 \times 40$	50	25	30	82	0.241	12.28	1.60
T150-4		100	75		58	0.278	10.76	5.30
T150-5		0	0		48	0.536	2.07	∞

Captions of Figures

Fig. 1. Specimen geometry and experimental set-up under FPS

Fig. 2. Experiment set-up: (a) Speckle pattern on specimen surface; (b) DIC set-up; and (c) Measurement devices under FPS

Fig. 3. Computational grids for Specimen L150-1

Fig. 4. Displacements along Line MN on Specimen L 120-1 when $P = 96.7\%P_{max}$: (a) Opening displacement; and (b) Sliding displacement

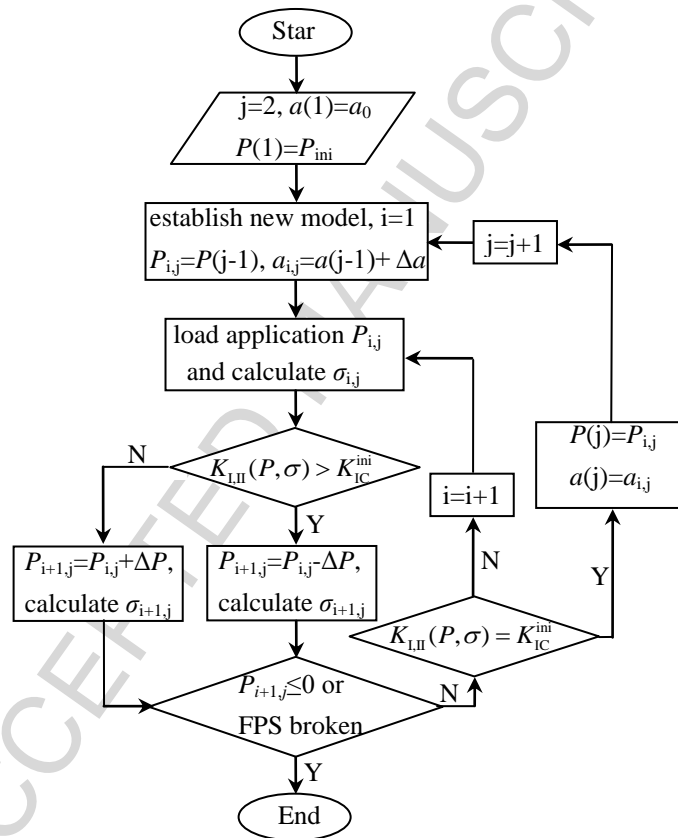**Fig. 5.** Bilinear σ-w concrete softening curve

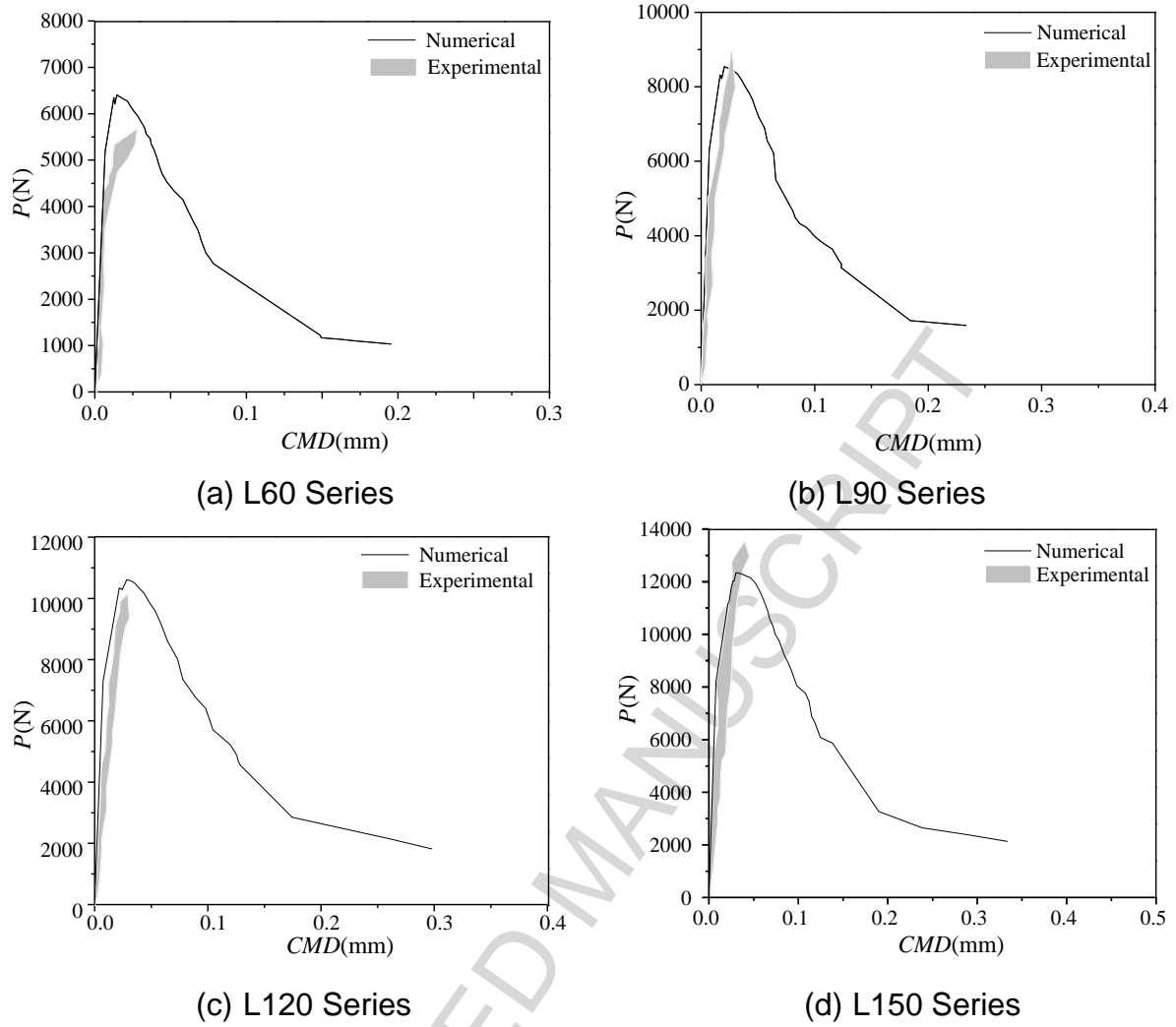**Fig. 6.** Program flow diagram for the numerical method

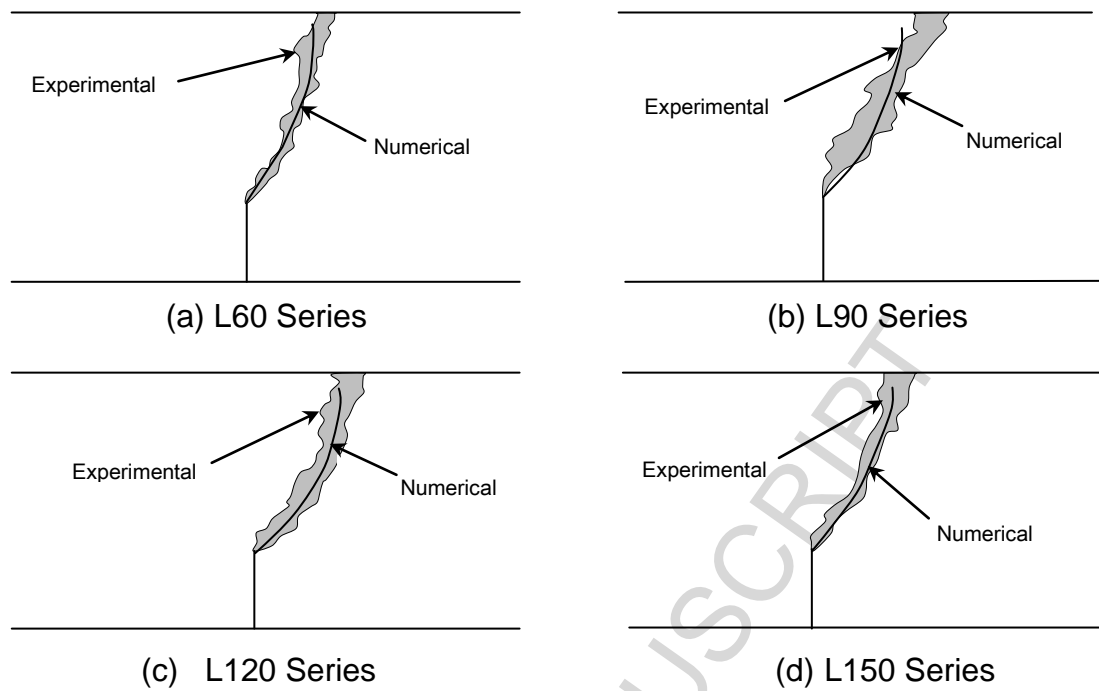**Fig. 7.** Numerical and experimental P-CMD curves for the four groups of beams with various heights: (a) L60 Series; (b) L90 Series; (c) L120 Series; and (d) L150 Series

Fig. 8. Numerical and experimental crack trajectories for the four groups of beams with various heights: (a) L60 Series; (b) L90 Series; (c) L120 Series; and (d) L150 Series

Fig. 9. FPZ evolution and crack opening/sliding displacements of Specimen L60-1: (a) $P = 74.9\%P_{max}$; (b) $P = 85.7\%P_{max}$; (c) $P = 92.6\%P_{max}$; (d) $P = P_{max}$; and (e) Shape of final macro-crack

Fig. 10. FPZ evolution and crack opening/sliding displacements of Specimen L90-1: (a) $P = 78.9\%P_{max}$; (b) $P = 89.4\%P_{max}$; (c) $P = 98.6\%P_{max}$; (d) $P = P_{maxc}$; and (e) Shape of final macro-crack

Fig. 11. FPZ evolution and crack opening/sliding displacements of Specimen L120-1: (a) $P = 76.5\%P_{max}$; (b) $P = 88.4\%P_{max}$; (c) $P = 96.7\%P_{max}$; (d) $P = P_{max}$; and (e) Shape of final macro-crack

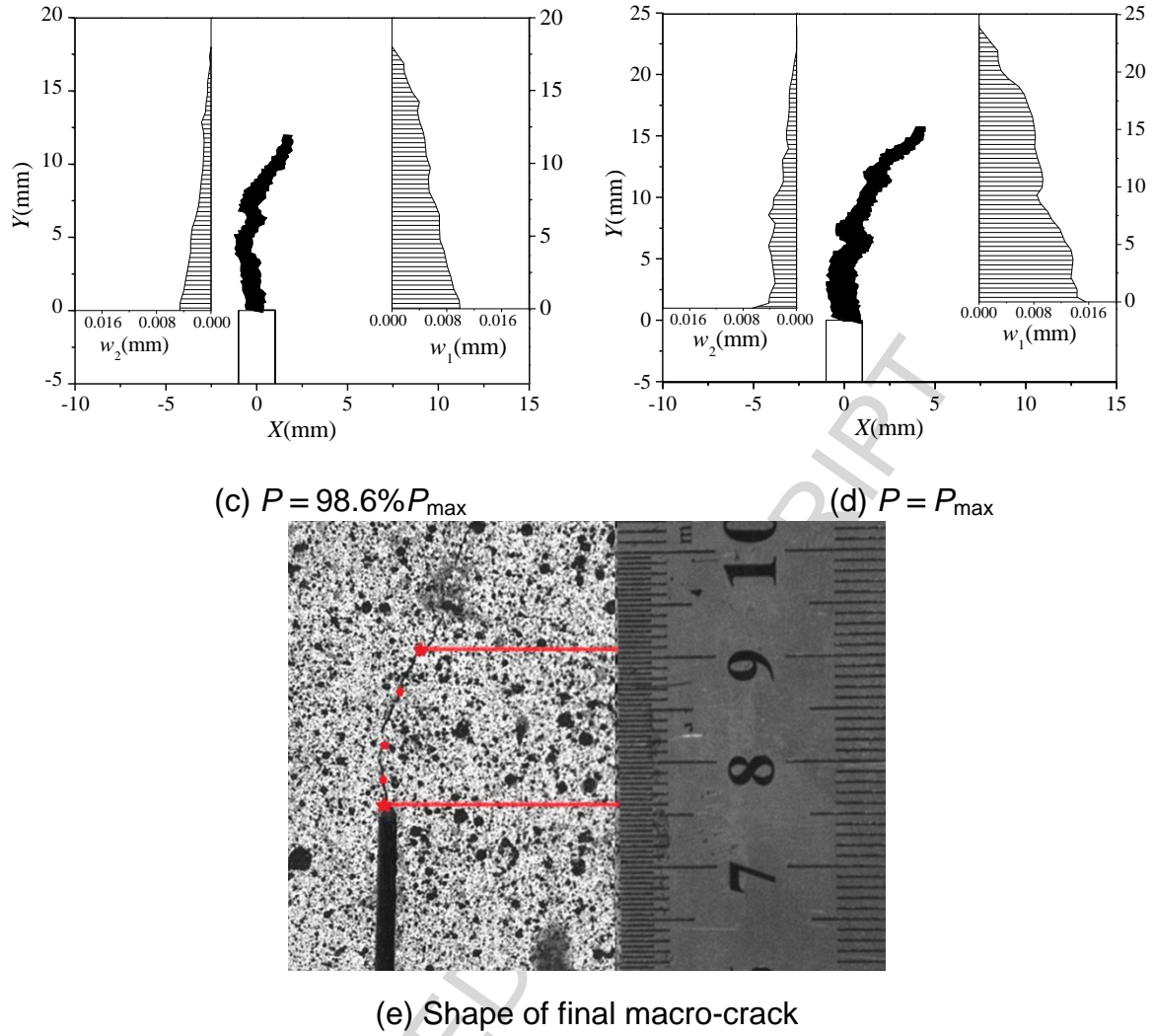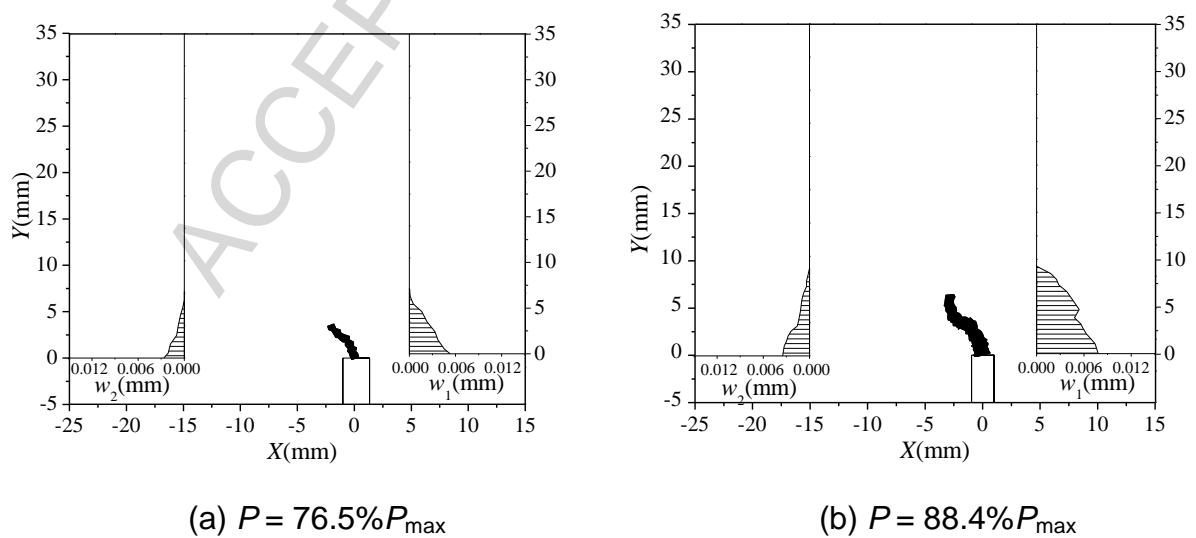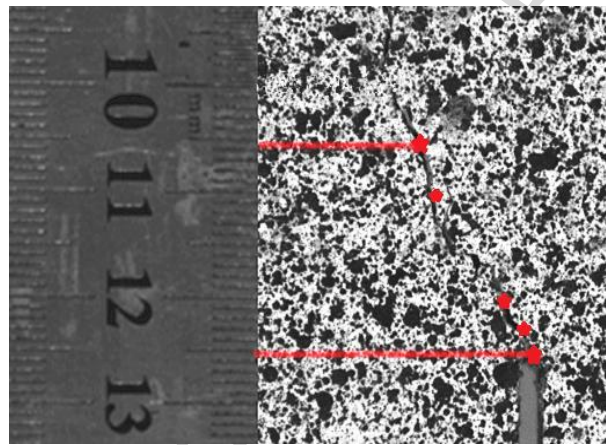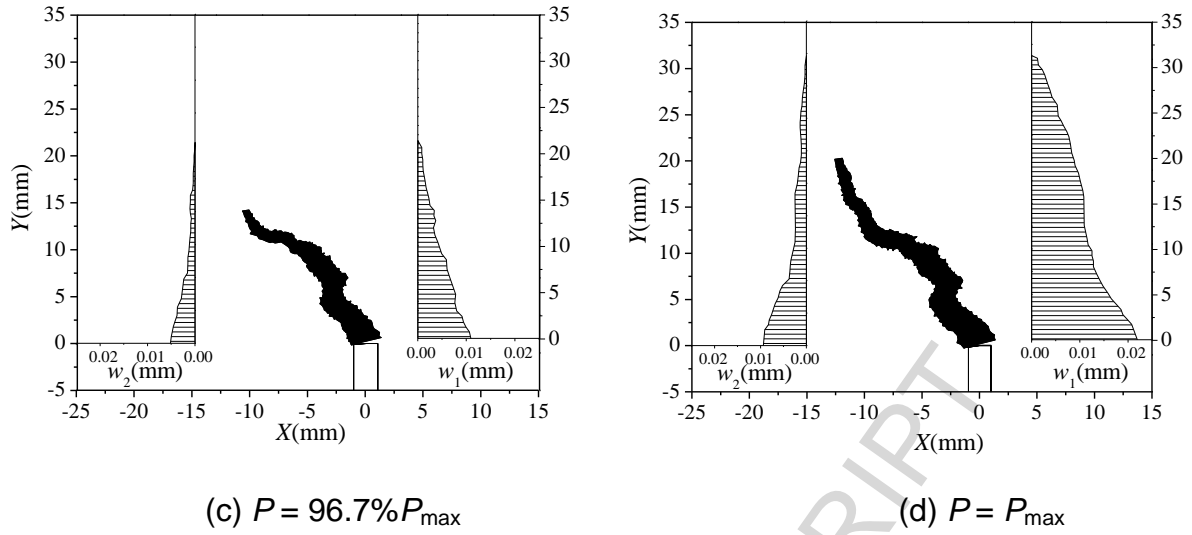**Fig. 12.** FPZ evolution and crack opening/sliding displacements of Specimen L150-1: (a) $P = 73.8\%P_{max}$; (b) $P = 90.8\%P_{max}$; (c) $P = 96.7\%P_{max}$; (d) $P = P_{max}$; and (e) Shape of final macro-crack

Fig. 13. *CTSD* vs. *CTOD* relationship

Fig. 14. $L_{FPZ}/(H\text{-}a_0)$ at peak load for various specimen sizes

Fig. 15. FPZ evolution for L-Series specimens

Fig. 16. FPZ evolution for S-Series specimens

Fig. 17. FPZ evolution for the specimens with varied ligament lengths

Fig. 18. FPZ evolution for T-Series specimens

Appendix II Figure
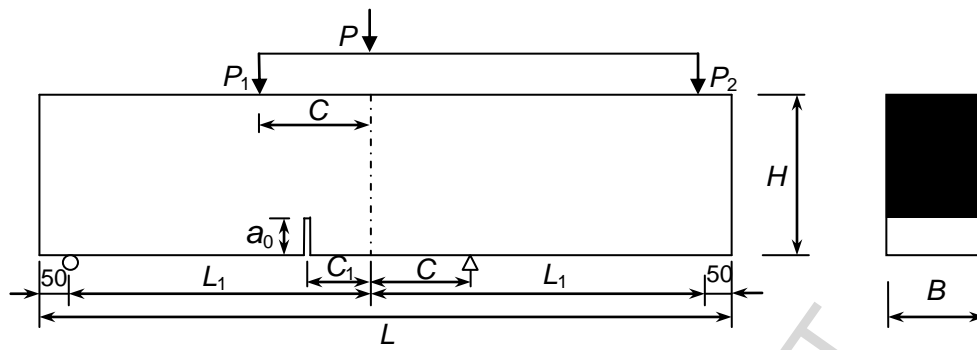
Fig. 1. Specimen geometry and experimental set-up under FPS

(a) Speckle pattern on specimen surface

(b) DIC set-up

(c) Measurement devices under FPS

Fig. 2. Experiment set-up
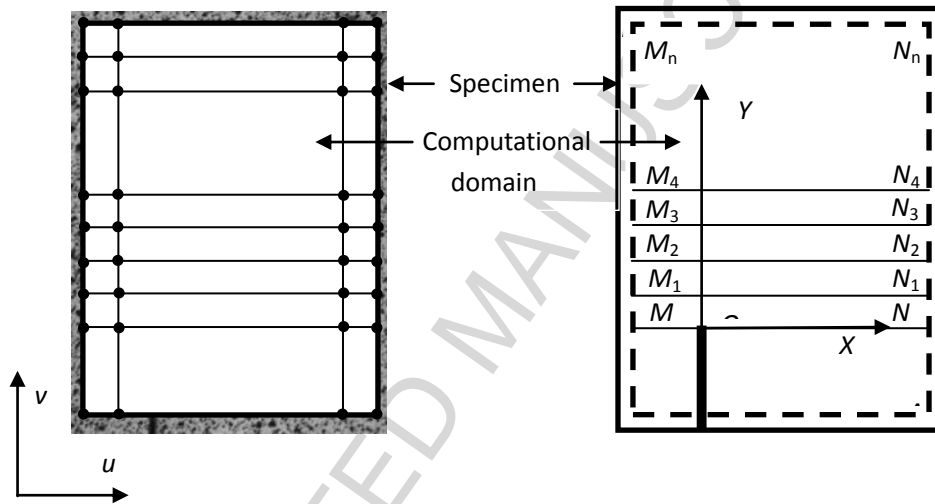
Fig. 3. Computational grids for Specimen L150-1
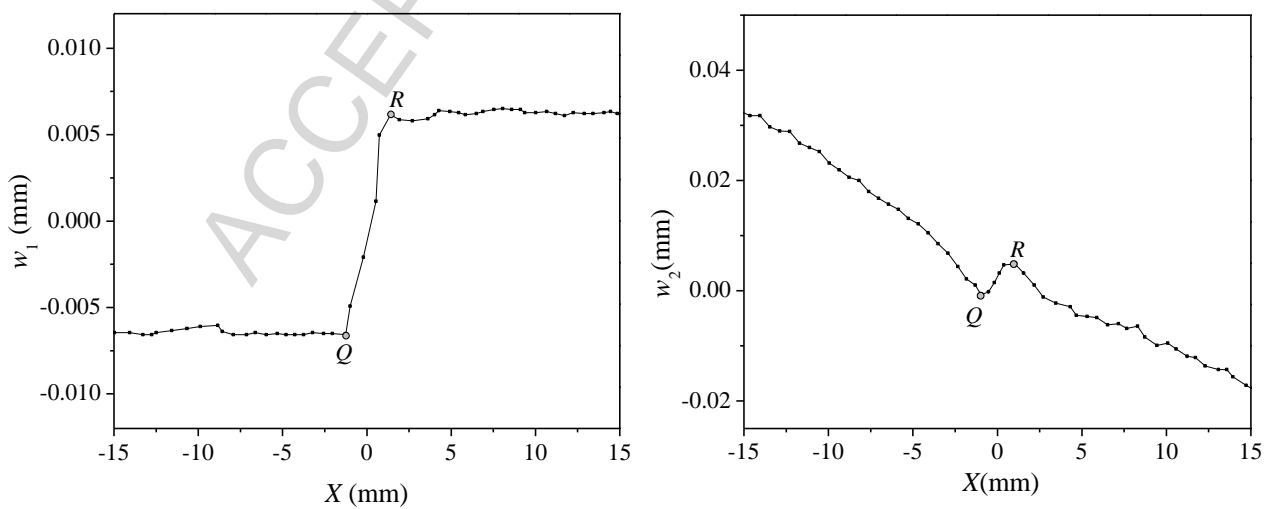
(a) Opening displacement

(b) Sliding displacement

Fig. 4. Displacements along Line MN on Specimen L120-1 when $P = 96.7\% P_{max}$
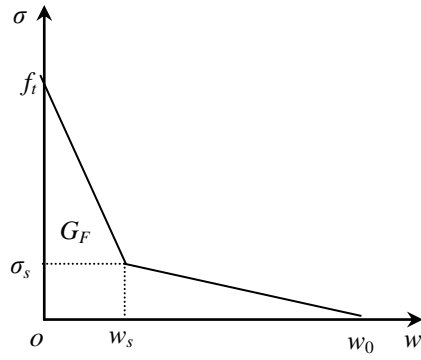
Fig. 5. Bilinear σ-w concrete softening curve

Fig. 6. Program flow diagram for the numerical method

Fig. 7. Numerical and experimental *P-CMD* curves for the four groups of beams with various heights

(a) L60 Series

(b) L90 Series

(c) L120 Series

(d) L150 Series

Fig. 8. Numerical and experimental crack trajectories for the four groups of beams with various heights

(a) $P = 74.9\%P_{max}$

(b) $P = 85.7\%P_{max}$

(c) $P = 92.6\%P_{max}$

(d) $P = P_{max}$
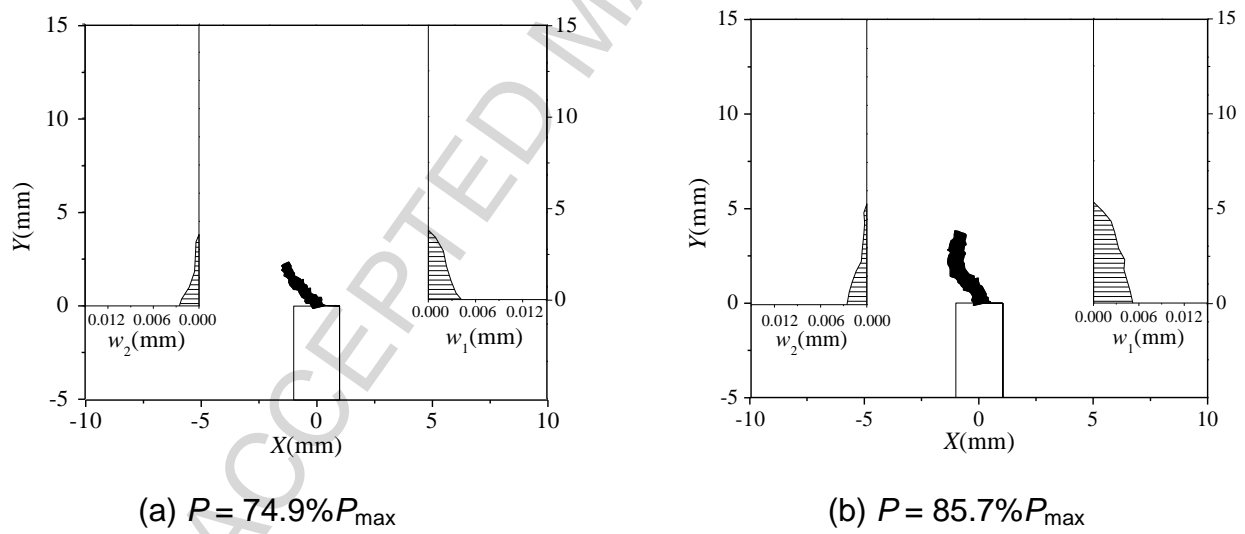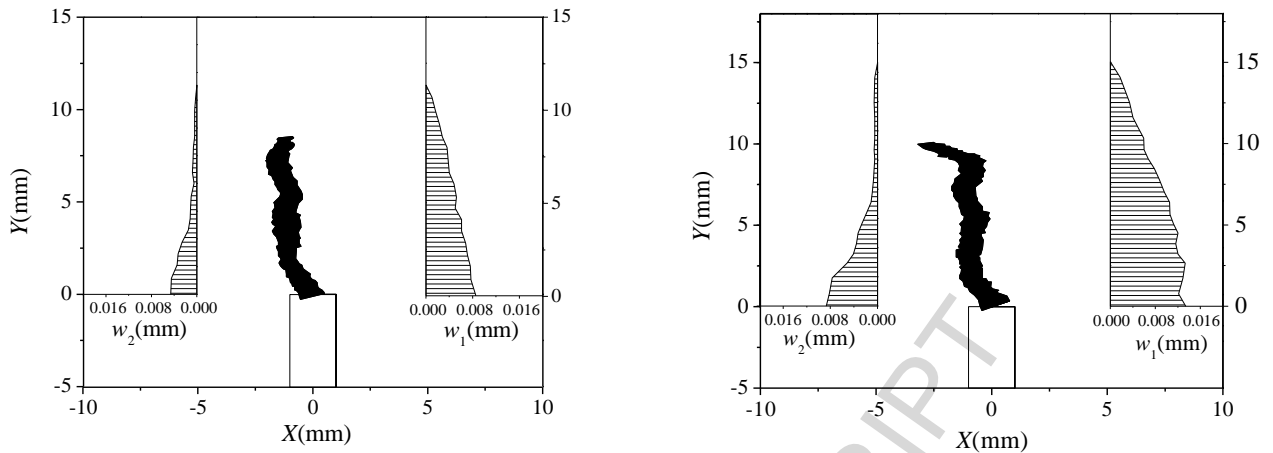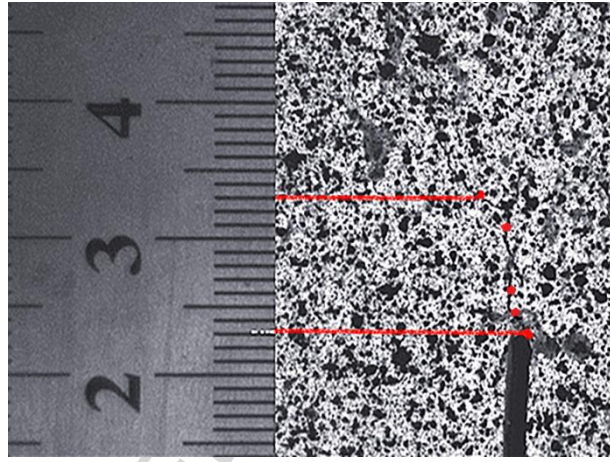
(e) Shape of final macro-crack

Fig. 9. FPZ evolution and crack opening/sliding displacements of Specimen L60-1
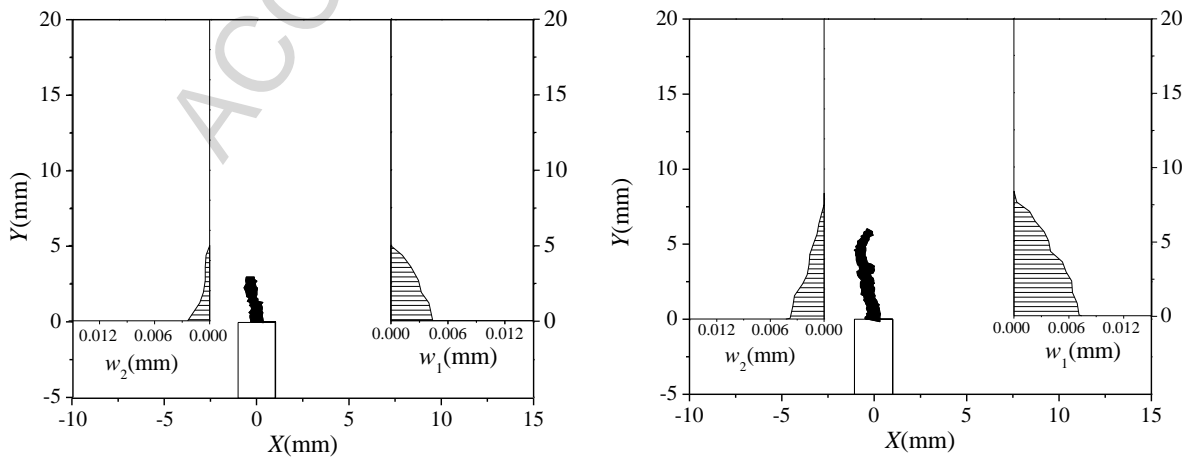
(a) $P = 78.9\%P_{max}$

(b) $P = 89.4\%P_{max}$

(c) $P = 98.6\%P_{max}$

(d) $P = P_{max}$

(e) Shape of final macro-crack

Fig. 10. FPZ evolution and crack opening/sliding displacements of Specimen L90-1

(a) $P = 76.5\%P_{max}$

(b) $P = 88.4\%P_{max}$

(c) $P = 96.7\%P_{max}$

(d) $P = P_{max}$

(e) Shape of final macro-crack

Fig. 11. FPZ evolution and crack opening/sliding displacements of Specimen L120-1

(a) $P = 73.8\%P_{max}$

(b) $P = 90.8\%P_{max}$

(c) P=96.7%P_{max} (d) P=P_{max}
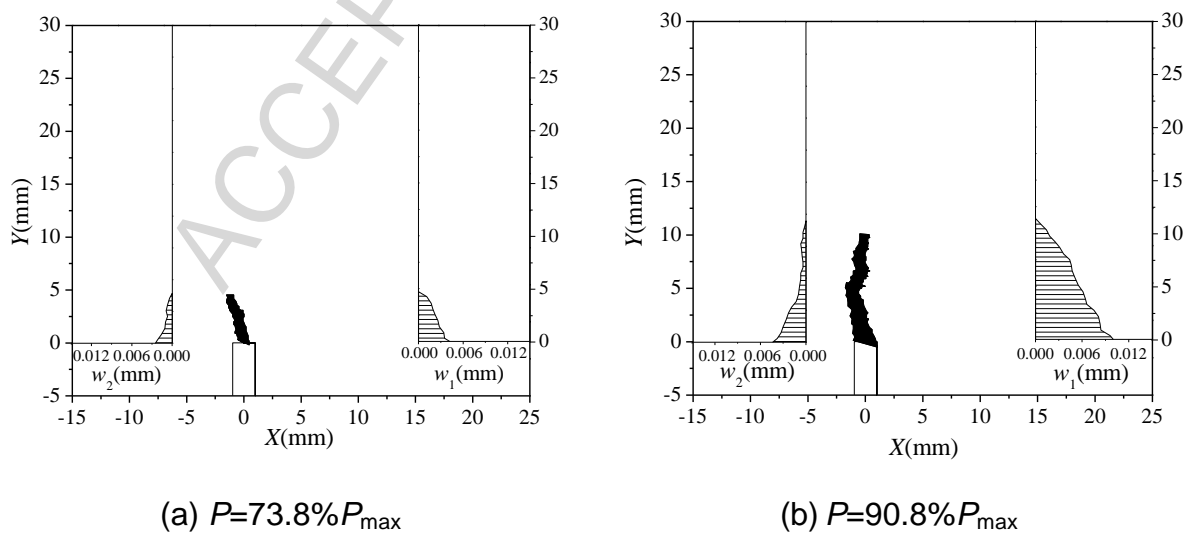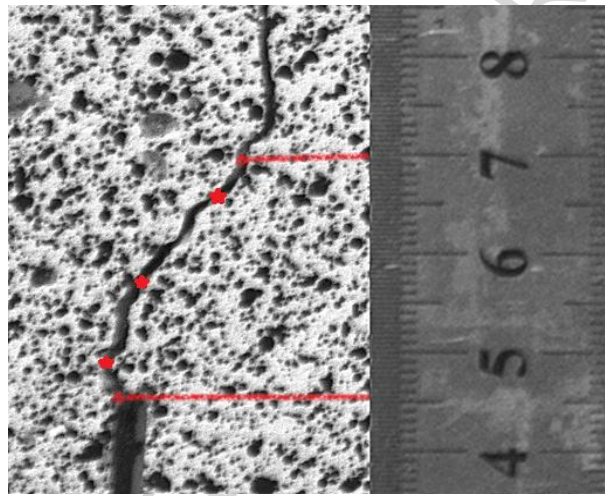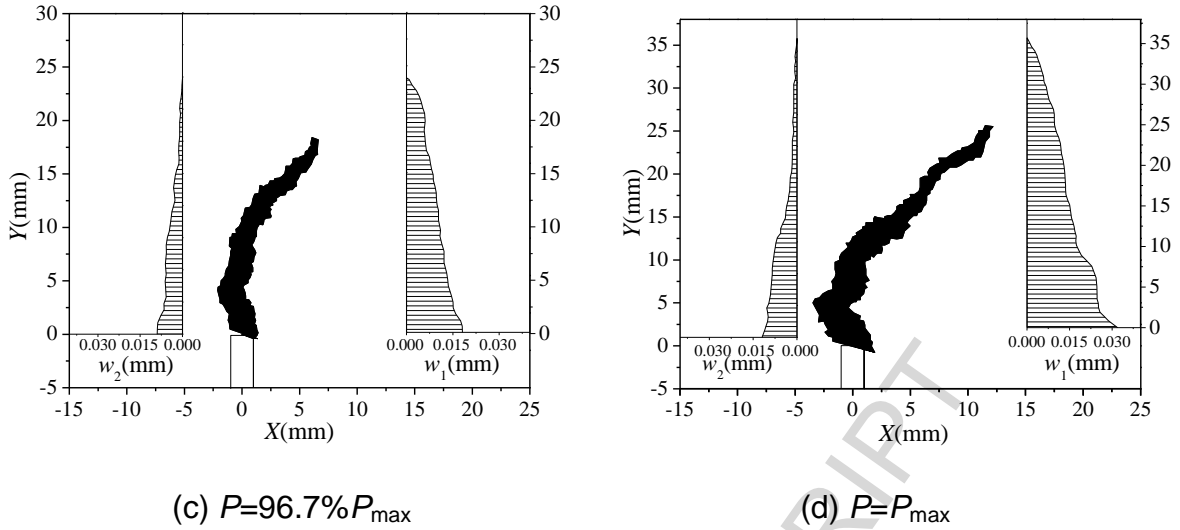
(e) Shape of final macro-crack

Fig. 12. FPZ evolution and crack opening/sliding displacements of Specimen L150-1
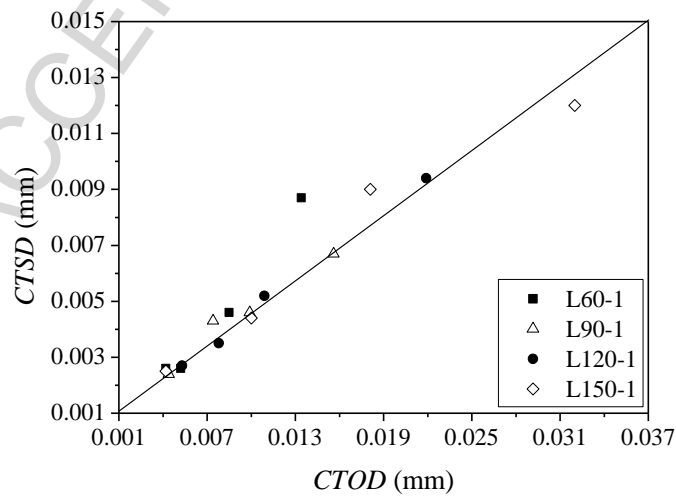
Fig. 13. *CTSD* vs. *CTOD* relationship
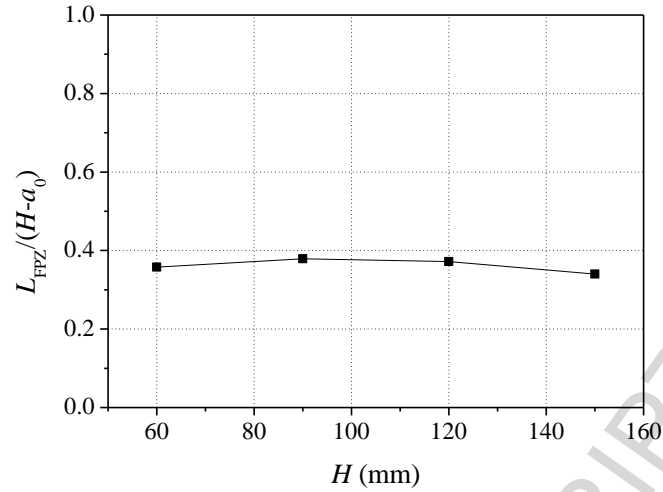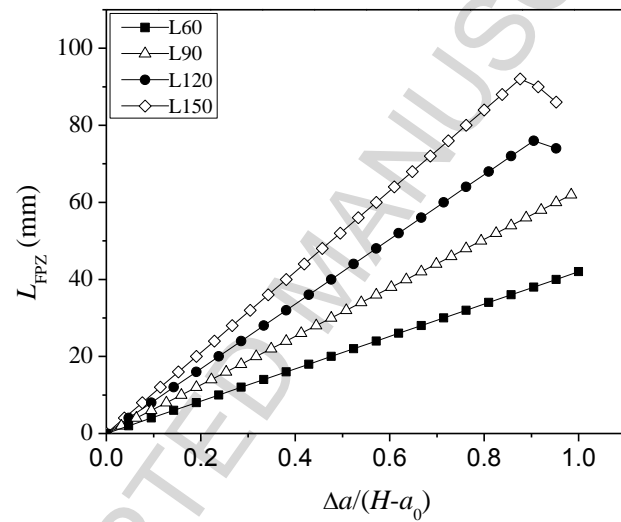
Fig. 14. $L_{\text{FPZ}}/(H\text{-}a_0)$ at peak load for various specimen sizes

Fig. 15. FPZ evolution for L-Series specimens
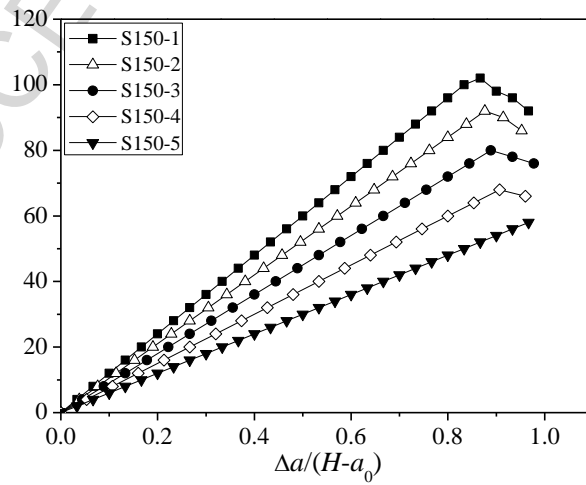
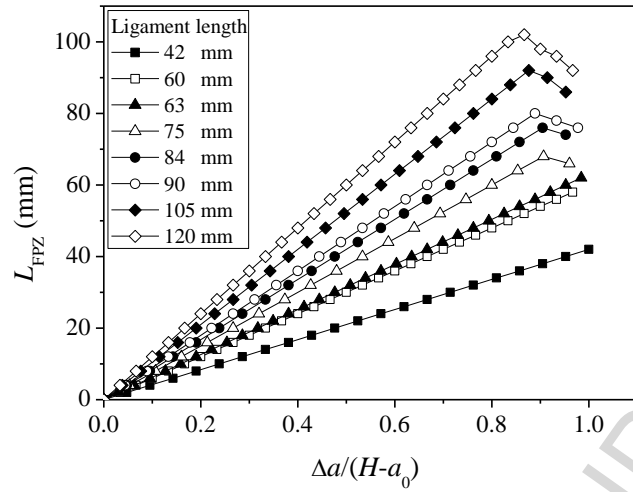**Fig. 16.** FPZ evolution for S-Series specimens

Fig. 17. FPZ evolution for the specimens with varied ligament lengths
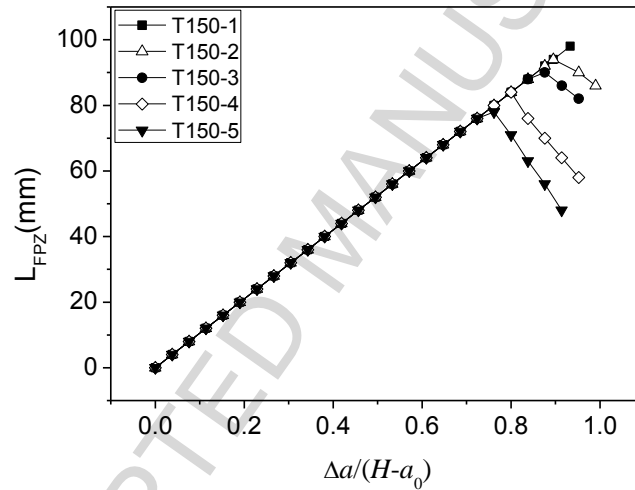

Fig. 18. FPZ evolution for T-Series specimens

Highlights

- DIC is used to study crack propagation of mixed mode fracture in concrete.

- A numerical method based on initial toughness is employed to study FPZ evolution.

- *CMOD*/*CMSD* remains approximately constant before P_{max}.

- FPZ evolution is influenced by the ligament length and K_I^{ini}/K_{II}^{ini}.

- FPZ cannot fully develop for small ligament length and mode II dominated fracture.